Numerical Experiments on Effect of Topographical Slope Changes in the Dynamics of Landslide Generated Water Waves and Submarine Mass Flows

J. Kafle[1], P. Kattel[2] [†], P. R. Pokhrel[3] and K. B. Khattri[4]

[1] Central Department of Mathematics, Tribhuvan University, Kathmandu, Nepal
[2] Department of Mathematics, Tri-Chandra Multiple Campus, Tribhuvan University, Kathmandu, Nepal
[3] Department of Mathematics, R R Campus, Tribhuvan University, Kathmandu, Nepal
[4] Department of Mathematics, School of Science, Kathmandu University, Kavre, Nepal

†*Corresponding Author Email*: *pkattel526@gmail.com*

ABSTRACT

When gravitational mass flows hit water bodies, they create water waves, called tsunami. The slopes of the mountain flanks surrounding a glacial lake or the slopes of the side walls of artificially constructed reservoirs play important roles in the intensity of splash on landslide impact, amplitudes and propagation speeds of the resulting water waves and possible dam breaching or overspilling of water. The proper analyses of such dynamics are useful for the possible mitigation measures. Here, we apply a general two-phase mass flow model to perform several numerical experiments and present geometrically three-dimensional, high-resolution simulation results for rapidly moving two-phase landslide/debris flow down a plane with varying slopes at its different parts, impacting a fluid reservoir. First, the upstream slope is kept constant; later to make it closer to reality, sudden changes in slopes are imposed one after another at different parts of the topography. The results focus on the effects of the sudden slope changes in the formation and propagation of dynamically different solid- and fluid wave-structures in the reservoir. Results show that steeper upper part of the topography produces more highly intensified tsunami that propagates more longitudinally than the steeper lower part. Thus, steeper upper parts need stronger right coast and steeper lower parts demand stronger side walls in mountain reservoirs to withstand the wave impacts. The results may help for the proper modeling of landslide and debris induced mountain tsunamis in rapidly changing slopes, the dynamics of turbidity currents and sediment transports in fluid reservoirs in high mountain slopes.

Keywords: Two-phase mass flows; Submarine landslides; Debris flows; Tsunami; Slope changes.

NOMENCLATURE

A	mobility number		m_{i_j}	$i{=}x,y; j{=}f,s$ fluxes
$b = b(x,y)$	basal topography		N_R	quasi-Reynolds number
C_{DG}	generalized drag coefficient		N_{R_A}	mobility Reynolds number
C	virtual mass coefficient		P	interpolation parameter for drag
f ; s	fluid phase; solid phase			
f,g	vectors of transport fluxes		p_{b_f}, p_{b_s}	effective fluid, solid pressures at base
F , G	fluid, solid-like drag contributions			
g^x, g^y, g^z	components of gravity		Re_p	particle Reynolds number
h	debris flow depth		$S_{x_f}, S_{x_s}, S_{y_f}, S_{y_s}$	source terms
h_f, h_s	fluid, solid phase depth			
H,L	typical height, extent of a debris flow		**T**	vector of conservative variables
			t;x,y,z	time; space coordinates
K_x, K_y	earth pressure coefficients		u_f, u_s, v_f, v_s	velocity components
M	a parameter for Reynolds number		**W**	vector of conservative state variables

x_b	position of bottom of slope	ζ, ζ_1, ζ_2	inclinations of basal topographies
x_{lc}	reservoir's left end position	η_f	fluid viscosity
		$\mu = \tan\delta$	basal friction coefficient
α_f, α_s	fluid, solid volume fractions	ξ	vertical distribution of
$\beta_{x_f}, \beta_{x_s}, \beta_{y_f}, \beta_{y_s}$	lateral hydraulic pressures	ρ_f, ρ_s	fluid, solid densities
γ	density ratio	χ	vertical shearing of fluid viscosity
δ, ϕ	basal, internal friction angles	$\frac{\partial}{\partial t}, \frac{\partial}{\partial x}, \frac{\partial}{\partial y}$	partial differential operators
ε	aspect ratio		

1. INTRODUCTION

Mass flows in geophysical contexts, like subaerial and submarine landslides and, in particular, debris flows are effectively two-phase flows of solid particles mixed with viscous fluid, and are very important sediment transport mechanisms (Pitman and Le 2005; Pudasaini 2012; Pudasaini 2014; Kafle 2019; Kattel 2019). From the environmental and industrial perspectives, advanced knowledge of the evolutions and dynamics of solid and fluid-phases, in particular, in landslides around coastal areas and particle transport in hydraulic plants is very important to estimate the velocity, kinetic energy, momentum and pressure for adopting the appropriate mitigation strategies (Pudasaini 2014). Submarine or subaqueous landslides are commonly observed as a mass wasting process that constitute one of the most important mechanisms for sediment transport which contribute substantially in shaping landscape margins of coastal regions (Kafle 2019). Although many research works have been focused on evaluating the landslide-induced tsunami generation and risks using statistical methods and empirical formulas, there is a lot yet to be studied about tsunami or water waves and submarine mass flow dynamics, and deposits in hydraulic channels and hydropower plants in mountainous regions employing the physical mathematical models, and robust numerical methods (Kafle 2014; Pudasaini 2014; Kafle 2019).

The big mountain rivers, lakes, glacial lakes, several artificial reservoirs, and also hydro-electric power plants situated at high mountain regions in the world are susceptible for landslide impact potentially creating water waves (Shrestha *et al.* 2010; Miao *et al.* 2014). Figure 1, as an example, is a picture of the flood due to the detachment and collapse of the rock-ice wall in Mt. Annapurna IV and the subsequent landslide and avalanche on May 5, 2012. The fluidized debris flow later turned into a debris flood and mud flow when it plunged into and mixed with the upstream source of the Seti River, Pokhara valley, in Kaski District, Nepal. The flood claimed 71 lives and swept away many houses around the river banks downstream (Kattel 2014). There are some more events in Nepal, e.g., the Jure landslide of August 2, 2014 in the central-north Nepal, and other avalanches and landslides in Mount Langtang and Everest areas triggered by the 2015 Gorkha earthquakes (April 25 and May 12) (Kafle *et al.* 2016; Kafle 2019). Some other events are 1958

Lituya Bay Megatsunami (Alaska) generated by an earthquake-induced landslide and the 1963 Vajont landslide (Italy) induced megatsunami (von Hardenberg 2011; Ward and Day 2011; Kafle 2019). Such events highlight the increasing interests for the fundamental, scientific and technological research in the relevant field in the Himalaya and also the need to design appropriate mitigation measures, hazard mappings and future planning (Masson *et al.* 2006).

Tsunamis are long water waves created by some sudden disturbances of the floor, surface or the banks of water body (Mohammed and Fritz 2012; Kafle 2014; Ma *et al.* 2015; Douglas 2016; Kafle *et al.* 2016; Kafle 2019; Kafle *et al.* 2019). Among the tsunamis caused by different geophysical triggering factors, landslide-generated tsunamis are more localized, thereby causing more local threats as compared to earthquake-generated tsunamis (Sammarco and Renzi 2008; Viroulet *et al.* 2013; Ma *et al.* 2015). Research in landslide generated tsunamis are very important for the safety of lives and infrastructures near the potential impact areas and construction of artificial reservoirs in mountains and valleys (Miao *et al.* 2014; Kafle 2019). The study of such events and the mitigation measures require physically-based models, efficient numerical tools and appropriate simulation techniques and strategic optimization of the defense measures (Pudasaini 2014; Kafle *et al.* 2016; Kattel *et al.* 2018; Mergili *et al.* 2018; Kafle *et al.* 2019).

Subaerial as well as submarine debris flows are generally gravity-driven multiphase (at least two-phase) flows that constitute solid grains mixed with viscous fluid. The rheology and flow behaviour are largely controlled by the material composition. Researches in recent years are found to focus on different aspects of single- and two-phase landslides, debris avalanches and debris flows, and induced tsunami among which Pudasaini (2012) made an advancement by developing a general two-phase mass flow model down a channel that accounts for strong interactions between the constituent phases, incorporating buoyancy and other three dominant physical aspects of virtual mass force, generalized drag and enhanced non-Newtonian viscous stress induced by the changing sediment concentration in the debris mixture during the flow.

Pitman and Le (2005) developed a two-fluid model that includes simple drag force to describe unsteady and non-uniform flows as a mixture of the solid particles and the fluid. In the two-layered model of

Fig. 1. View of the Seti River in Kharapani, Kaski District, Western Nepal, after the destruction by the debris and mud flow of May 5, 2012. Left: During the flood, some houses are seen on the bank of the river. Right: After the flood, the houses were swept away (Kattel 2014).

Jiang and LeBlond (1993), the deformable subaquaous landslide and associated tsunami waves were dynamically coupled. Ma *et al.* (2012) presented a shock-capturing three-dimensional nonhydrostatic dispersive surface wave model. Ma *et al.* (2015) presented a depth-averaged computational model for two-layer granular landslide and tsunami waves generation. Grilli *et al.* (2007) carried out numerical simulations to assess coastal tsunami hazards by performing tsunami simulations with the Boussinesq long wave model. Based on dimensional analysis and experimental data, Slingerl and Voight (1979) proposed an empirical logarithmic-equation for maximum wave amplitude as a function of landslide kinetic energy and water depth. Walder *et al.* (2003) demonstrated that the shape and height of the generated wave in near field depend on the water depth, the volume of the slide and the duration of the submerged landslide motion. Behroozi and Vaghefi (2020) considered the effects of fluid compressibility and energy depreciation in the reservoir boundaries by introducing a mesh free numerical model for the simulation of hydrodynamic response of dam-reservoir-foundation system. Kuswandi and Triatmadja (2019) elaborated the use of a dam break system to generate a surge model for the study of tsunami runup, run-down and scouring around a vertical cylinder.

The two-phase debris flows were simulated by Pudasaini (2012) for the first time for the explicit evolution of the solid and fluid phases as the subaerial debris mass collapses and slides down the slopes. Furthermore, Pudasaini (2014) simulated geometrically two-dimensional flows in which the two-phase subaerial debris flows impact the still reservoir downstream to produce tsunami at impact and the submarine debris mass slides along the bathymetric surface of the reservoir. For idealized

geometry, Kafle (2014) further presented simulation results for two-phase and geometrically three-dimensional subaerial flows impacting a fluid reservoir and observed some natural phenomena for the first time by using two-phase debris flow model (Pudasaini 2012). Kafle *et al.* (2016) further simulated two-phase and three-dimensional subaerial flows impacting a fluid reservoir, and the effects of the position of initial debris mass on the splash, tsunami generation and submarine debris mass movements along with impact and submergence times and scalings. The submerge time scaling for a deformable two-phase debris was found to deviate substantially from the same for a non-deformable solid. Mergili *et al.* (2018) studied the complex hydro-geomorphic process chains in a multi-lake outburst flood in the Santa Cruz Valley in Cordillera Blanca, Peru. Kafle and Tuladhar (2018) presented and discussed a simulation related to a partially submerged landslide impacting a quiescent reservoir. Through computational experiments, Kattel *et al.* (2018) analyzed different types of flow-obstacle-interactions including debris vacuum generation, flow obstruction, redirection and phase-separation. Kafle *et al.* (2019) presented geometrically three-dimensional simulation results for a two-phase debris mass impacting a fluid reservoir containing obstacles of different sizes, dimensions and numbers, installed at different positions both in subaerial slopes and in bathymetric surface. Kafle and Kattel (2019) focused on the symmetric issues in the flow in different rotational symmetries and the obstacle shapes employing the general two-phase mass flow model (Pudasaini 2012) and the open source computational tool r.avaflow. Qiao *et al.* (2018) also used the same model to simulate and analyze the run out characteristics of the catastrophic landslide that occurred in 2015 at Hongao construction waste

dumpsite in the Guangming New District of Shenzhen, China. The two-phase mass flow model (Pudasaini 2012) is also employed to construct a generalized quasi two-phase bulk mixture model Pokhrel *et al.* (2018), and an extended quasi-two phase mixture model (Khattri and Pudasaini 2018) capturing more physics of two-phase mass flows. The model equations are further modified in terms of stream function vorticity-formulation for mixture mass flow by Pokhrel and Pudasaini (2020).

In most of the existing works, numerical experiments were carried on by taking constant upstream slope (Pudasaini 2012; Kafle 2014; Pudasaini 2014; Kafle *et al.* 2016; Kattel *et al.* 2016; Kafle and Tuladhar 2018; Kattel *et al.* 2018; Qiao *et al.* 2018; Kafle 2019; Kafle *et al.* 2019). This may not be the case in many real field scenarios. Figure 2, as an example of sudden slope changes in the topography in the mountain flanks around the Everest Gokyo Lake. The slopes of the mountain flanks surrounding a glacial lake or the slopes of the side walls of artificially constructed reservoirs play important roles in the degree or intensity of splash on impact, amplitudes and propagation speeds of the resulting water waves and possible dam breaching or overspilling of water. Making the topography much closer to reality, here we present simulations for the cases with different sudden slope changes in the topography. The simultaneous dynamics of the two-phase and geometrically three-dimensional subaerial and submarine landslide or debris flow, the resulting tsunami generation and propagation upon debris impact at a fluid reservoir or a lake, the subsequent submarine debris flow, turbidity current, particle transport, and the analyses of different types of waves and their complex interactions are presented in this work imposing different slope changes in different parts of the topography.

Fig. 2. The Everest Gokyo Lake: Slope changes can be seen in the mountain flanks followed by the lake (Source: trekkingtrail.com).

2. PHYSICAL-MATHEMATICAL MODEL

2.1 Model Equations

Now, we briefly mention the employed general two-phase mass flow (Pudasaini 2012). The two phases (sediments and viscous fluid) are described by their different material properties. The fluid phase is characterized by its material density ρ_f, viscosity η_f and isotropic stress distribution. The solid phase is characterized by its material density ρ_s, internal friction angle ϕ, the basal friction angle δ, and an anisotropic stress distribution through the lateral earth pressure coefficient K. In the following model equations (1)-(6), x, y and z are coordinates along the downslope, cross-slope and the surface normal directions, respectively with g^x, g^y and g^z as the respective components of gravitational acceleration. The subscripts s and f stand for the solid and the fluid phases, and $\mathbf{u}_f = (u_f, v_f)$ and $\mathbf{u}_s = (u_s, v_s)$ are the depth-averaged velocity components for fluid and for solid in the downslope (x) and the cross-slope (y) directions, respectively. The flow depth is h; α_s is the solid-volume fraction in the mixture, so that $\alpha_f = 1 - \alpha_s$ is the fluid volume fraction. The depth-averaged non-linear partial differential equations representing mass ((3)-(4)), and momentum ((5)-(6)) balances for solid and fluid in the downslope and the cross-slope directions are given by (Pudasaini 2012):

$$\frac{\partial}{\partial t}(\alpha_s h) + \frac{\partial}{\partial x}(\alpha_s h u_s) + \frac{\partial}{\partial y}(\alpha_s h v_s) = 0, \qquad (1)$$

$$\frac{\partial}{\partial t}(\alpha_f h) + \frac{\partial}{\partial x}(\alpha_f h u_f) + \frac{\partial}{\partial y}(\alpha_f h v_f) = 0, \qquad (2)$$

$$\frac{\partial}{\partial t}\left[\alpha_s h(u_s - \gamma C(u_f - u_s))\right]$$

$$+ \frac{\partial}{\partial x}\left[\alpha_s h\left(u_s^2 - \gamma C(u_f^2 - u_s^2) + \frac{1}{2}\beta_{x_s} h\right)\right]$$

$$+ \frac{\partial}{\partial y}\left[\alpha_s h(u_s v_s - \gamma C(u_f v_f - u_s v_s))\right] = h S_{x_s}, \qquad (3)$$

$$\frac{\partial}{\partial t}\left[\alpha_s h(v_s - \gamma C(v_f - v_s))\right]$$

$$+ \frac{\partial}{\partial x}\left[\alpha_s h(u_s v_s - \gamma C(u_f v_f - u_s v_s))\right]$$

$$+ \frac{\partial}{\partial y}\left[\alpha_s h\left(v_s^2 - \gamma C(v_f^2 - v_s^2) + \frac{1}{2}\beta_{y_s} h\right)\right] = h S_{y_s}, \qquad (4)$$

$$\frac{\partial}{\partial t}\left[\alpha_f h\left(u_f + \frac{\alpha_s}{\alpha_f} C(u_f - u_s)\right)\right]$$

$$+ \frac{\partial}{\partial x}\left[\alpha_f h\left(u_f^2 + \frac{\alpha_s}{\alpha_f} C(u_f^2 - u_s^2) + \frac{1}{2}\beta_{x_f} h\right)\right]$$

$$+ \frac{\partial}{\partial y}\left[\alpha_f h\left(u_f v_f + \frac{\alpha_s}{\alpha_f} C(u_f v_f - u_s v_s)\right)\right] = h S_{x_f}, (5)$$

$$\frac{\partial}{\partial t}\left[\alpha_f h\left(v_f+\frac{\alpha_s}{\alpha_f}C(v_f-v_s)\right)\right]$$

$$+\frac{\partial}{\partial x}\left[\alpha_f h\left(u_f v_f+\frac{\alpha_s}{\alpha_f}C(u_f v_f-u_s v_s)\right)\right]$$

$$+\frac{\partial}{\partial y}\left[\alpha_f h\left(v_f^2+\frac{\alpha_s}{\alpha_f}C(v_f^2-v_s^2)+\frac{1}{2}\beta_{y_f}h\right)\right]=hS_{y_f}, (6)$$

in which $\beta_{x_s}=\varepsilon K_x p_{b_s}$, $\beta_{y_s}=\varepsilon K_y p_{b_s}$, $\beta_{x_f}=\beta_{y_f}=\varepsilon p_{b_f}$, $p_{b_f}=-g^z$, $p_{b_s}=(1-\gamma)p_{b_f}$. Here, p_{b_f} and p_{b_s} are the effective fluid and solid pressures at the base. γ is the ratio of fluid density to the solid density, C is the virtual mass coefficient (enhanced kinetic energy of the fluid phase induced by solid particles).

The source terms in the right hand sides of the Eqs. (3)-(6) are (Pudasaini 2012):

$$S_{x_s}=\alpha_s\left[g^x-p_{b_s}\left(\frac{u_s}{|\mathbf{u_s}|}\tan\delta+\varepsilon\frac{\partial b}{\partial x}\right)\right]-\varepsilon\alpha_s\gamma p_{b_f}$$

$$\cdot\left[\frac{\partial h}{\partial x}+\frac{\partial b}{\partial x}\right]+C_{DG}(u_f-u_s)\left|\mathbf{u}_f-\mathbf{u}_s\right|^{J-1}, \qquad (7)$$

$$S_{y_s}=\alpha_s\left[g^y-p_{b_s}\left(\frac{v_s}{|\mathbf{u_s}|}\tan\delta+\varepsilon\frac{\partial b}{\partial y}\right)\right]-\varepsilon\alpha_s\gamma p_{b_f}$$

$$\cdot\left[\frac{\partial h}{\partial y}+\frac{\partial b}{\partial y}\right]+C_{DG}(v_f-v_s)\left|\mathbf{u}_f-\mathbf{u}_s\right|^{J-1}, \qquad (8)$$

$$S_{x_f}=\alpha_f\left[g^x-\varepsilon\left[\frac{1}{2}p_{b_f}\frac{h}{\alpha_f}\frac{\partial\alpha_s}{\partial x}+p_{b_f}\frac{\partial b}{\partial x}\right.\right.$$

$$-\frac{1}{\alpha_f N_R}\left\{2\frac{\partial^2 u_f}{\partial x^2}+\frac{\partial^2 v_f}{\partial y\partial x}+\frac{\partial^2 u_f}{\partial y^2}-\frac{\chi u_f}{\varepsilon^2 h^2}\right\}$$

$$+\frac{1}{\alpha_f N_{R_{\mathcal{A}}}}\left\{2\frac{\partial}{\partial x}\left(\frac{\partial\alpha_s}{\partial x}(u_f-u_s)\right)\right.$$

$$+\frac{\partial}{\partial y}\left(\frac{\partial\alpha_s}{\partial x}(v_f-v_s)+\frac{\partial\alpha_s}{\partial y}(u_f-u_s)\right)\right\}$$

$$\left.\left.-\frac{\xi\alpha_s(u_f-u_s)}{\varepsilon^2\alpha_f N_{R_{\mathcal{A}}}h^2}\right]\right]-\frac{1}{\gamma}C_{DG}(u_f-u_s)\left|\mathbf{u}_f-\mathbf{u}_s\right|^{J-1}, (9)$$

$$S_{y_f}=\alpha_f\left[g^y-\varepsilon\left[\frac{1}{2}p_{b_f}\frac{h}{\alpha_f}\frac{\partial\alpha_s}{\partial y}+p_{b_f}\frac{\partial b}{\partial y}\right.\right.$$

$$-\frac{1}{\alpha_f N_R}\left\{2\frac{\partial^2 v_f}{\partial y^2}+\frac{\partial^2 u_f}{\partial x\partial y}+\frac{\partial^2 v_f}{\partial x^2}-\frac{\chi v_f}{\varepsilon^2 h^2}\right\}$$

$$+\frac{1}{\alpha_f N_{R_{\mathcal{A}}}}\left\{2\frac{\partial}{\partial y}\left(\frac{\partial\alpha_s}{\partial y}(v_f-v_s)\right)\right.$$

$$+\frac{\partial}{\partial x}\left(\frac{\partial\alpha_s}{\partial y}(u_f-u_s)+\frac{\partial\alpha_s}{\partial x}(v_f-v_s)\right)\right\}$$

$$\left.\left.-\frac{\xi\alpha_s(v_f-v_s)}{\varepsilon^2\alpha_f N_{R_{\mathcal{A}}}h^2}\right]\right]-\frac{1}{\gamma}C_{DG}(v_f-v_s)\left|\mathbf{u}_f-\mathbf{u}_s\right|^{J-1}, (10)$$

where $C_{DG}=\dfrac{\alpha_s\alpha_f(1-\gamma)}{[\varepsilon U_T\{PF(Re_p)+(1-P)G(Re_p)\}]^J}$,

$$\gamma=\frac{\rho_f}{\rho_s}, F=\frac{\gamma}{180}\left(\frac{\alpha_f}{\alpha_s}\right)^3 Re_p, G=\alpha_f^{M(Re_p)-1},$$

$$Re_p=\frac{\rho_f dU_T}{\eta_f}, N_R=\frac{\sqrt{gLH}\rho_f}{\alpha_f\eta_f}, N_{R_A}=\frac{\sqrt{gLH}\rho_f}{A\eta_f}. \qquad (11)$$

L and H are the typical length and depth of the flow, $\varepsilon=H/L$ is the aspect ratio, and $\mu=\tan\delta$ is the basal friction coefficient. The generalized drag coefficient C_{DG} is modeled by a linear combination with the interpolation parameter $P\in[0,1]$ of the solid-like (G) and fluid-like (F) drag contributions to flow resistance. $J=1$ or 2 represent simple linear or quadratic drag. U_T is the terminal velocity of a particle, M is a function of the particle Reynolds number (R_{e_p}), χ includes vertical shearing of fluid velocity, and ξ addresses different distributions of α_s. A is the mobility of the fluid at the interface, and N_R and N_{R_A} are respectively the quasi-Reynolds number and mobility-Reynolds number associated with the classical Newtonian and enhanced non-Newtonian fluid viscous stresses. Slope topography is given by $b=b(x,y)$.

2.2. Numerical Methods

It is very difficult to design laboratory experiments to replicate the real field events. The difficulty lies mainly in capturing the failure mechanism, and another difficulty lies in scaling. Moreover, it is extremely difficult to assess fields during the events. It is mainly due to the high momentum and kinetic energy of the flow. So, numerical experiments are the most promising and cost effective way to study such events (Kattel 2019). The above six Eqs. (1)-(6) can be written in a compact vectorial form:

$$\frac{\partial\mathbf{T(w)}}{\partial t}+\frac{\partial\mathbf{f(w)}}{\partial x}+\frac{\partial\mathbf{g(w)}}{\partial y}=\mathbf{s(w)}, \qquad (12)$$

where $\mathbf{w}=(h_s, h_f, m_{s_x}, m_{f_x}, m_{s_y}, m_{f_y})^T$, denotes the vector of conservative variables $h_s=\alpha_s h$, $h_f=\alpha_f h$ are the solid and fluid contributions to the debris depths (or heights); and $m_{s_x}=\alpha_s hu_s$, $m_{f_x}=\alpha_f hu_f$; $m_{s_y}=\alpha_s hv_s$, $m_{f_y}=\alpha_f hv_f$ are respectively the solid and fluid momenta in x- and y-directions. Then, $\mathbf{T(w)}$ is a vector with components as the terms inside $\frac{\partial}{\partial t}$ of (1)-(6). Also, $\mathbf{f(w)}$ and $\mathbf{g(w)}$ are the transport fluxes in the x- and y-directions, with terms inside $\frac{\partial}{\partial x}$ and $\frac{\partial}{\partial y}$ of (1)-(6) respectively, and $s(w)=(0,0,hS_{x_s},hS_{y_s},hS_{x_f},hS_{y_f})^T$ is the vector of the source terms from (7)-(10). After expressing the model in this standard, well-structured conservative

form, we directly apply the higher-order shock-capturing scheme, namely the Total Variation Diminishing Non-Oscillatory Central (TVD-NOC) difference scheme on it (Pudasaini and Hutter 2007; Pudasaini 2012).The discretization of the spatial and temporal domains are carried out with uniform stationary width Δx, Δy and Δt. The discrete mesh points will be denoted by (x_i, y_j, t^n) and are defined as $x_i = i\Delta x$, $i = 0,1,2,...;$ $y_j = j\Delta y$, $j = 0,1,2,...;$ $t^n = n\Delta t$, $n = 0,1,2,...$,where the mesh cell (x_i, y_j) has the boundaries $(x_{i\pm\frac{1}{2}}, y_{j\pm\frac{1}{2}})$, where $x_{i+\frac{1}{2}} = x_i + \frac{\Delta x}{2}$, etc.

The staggered averages at $(x_{i\pm1/2}, y_{j\pm1/2}, t^{n+1})$ are then computed by the cell averages at (x_i, y_j, t^n).

Now,

$$C_{i,j} = \left\{ (x,y) : |x - x_i| \le \frac{\Delta x}{2}, |y - y_j| \le \frac{\Delta y}{2} \right\}. \quad (13)$$

is the $(i, j)^{th}$ cell covered region. For $(x,y) \in C_{i,j}$, suppose $U_{i,j}^n$ denote the cell average over this region at time t^n. Then,

$$\tilde{w}_{i,j}(x,y,t^n) = U_{i,j}^n + \sigma_{i,j}^x(x - x_i) + \sigma_{i,j}^y(y - y_j) \quad (14)$$

is a piecewise linear reconstruction over the cell, where $\sigma_{i,j}^x$ and $\sigma_{i,j}^y$ respectively are the discrete slopes of U in the $x-$ and $y-$ directions which are determined by a TVD-limiter (minmod limiter, in our case) (Pudasaini and Hutter 2007). The cell average $w_{i+1/2, j+1/2}^{n+1}$ at $(x_{i+1/2}, y_{j+1/2}, t^{n+1})$ is given by (Pudasaini and Hutter 2007).

$$
\begin{aligned}
w_{i+1/2,j+1/2}^{n+1} = &\frac{1}{4}\left\{ w_{i,j}^n + w_{i+1,j}^n + w_{i+1,j+1}^n + w_{i,j+1}^n \right\} \\
&+ \frac{\Delta x}{16}\left\{ w_{i,j}^x - w_{i+1,j}^x - w_{i+1,j+1}^x + w_{i,j+1}^x \right\} \\
&+ \frac{\Delta y}{16}\left\{ w_{i,j}^y + w_{i+1,j}^y - w_{i+1,j+1}^y - w_{i,j+1}^y \right\} \\
&- \frac{\Delta t}{2\Delta x}\left\{ f\left(w_{i+1,j}^{n+1/2}\right) + f\left(w_{i+1,j+1}^{n+1/2}\right) - f\left(w_{i,j}^{n+1/2}\right) \right. \\
&\left. - f\left(w_{i,j+1}^{n+1/2}\right) \right\} - \frac{\Delta t}{2\Delta y}\left\{ g\left(w_{i,j+1}^{n+1/2}\right) + g\left(w_{i+1,j+1}^{n+1/2}\right) \right. \\
&\left. - g\left(w_{i,j}^{n+1/2}\right) - g\left(w_{i+1,j}^{n+1/2}\right) \right\} \\
&+ \frac{\Delta t}{4}\left\{ s\left(w_{i+1/4,j+1/4}^{n+1/2}\right) + s\left(w_{i+3/4,j+1/4}^{n+1/2}\right) \right. \\
&\left. + s\left(w_{i+3/4,j+3/4}^{n+1/2}\right) + s\left(w_{i+1/4,j+3/4}^{n+1/2}\right) \right\}.
\end{aligned}
$$

$$(15)$$

CFL condition is maintained for stability, and an appropriate limiter (minmod) is used to avoid spurious oscillations in the solution domains

(Pudasaini and Hutter 2007).

3. SIMULATING TWO-PHASE DEBRIS FLOW AND TSUNAMI

Here, we simulate the two-phase landslide (or debris flow) and the resulting tsunamis, and their interactions when the upstream slope is kept constant in the first, then to make it closer to reality, with a sudden slope changes in the sliding planes and analyze and compare the results among sudden slope changes, and also with the constant upstream slope.

3.1 Geometrical and Material Parameters

For all of our simulations, we consider a (geometrically) three-dimensional and two-phase subaerial debris flow that hits a fluid reservoir downstream. The upper part of the channel is inclined downwards to the right and is flat ($\zeta = 0^\circ$) in the lateral direction (Fig. 3). Thus, the slope angles for the entire flow domain is given by

$$\zeta = \begin{cases} \zeta_1 & for \quad 0 \le x \le 100m, \\ \zeta_2 & for \quad 100 < x \le x_b\, m, \\ 0 & for \quad x_b < x \le 300m. \end{cases}$$

where $x_b = 100 \times (1 + 1/\tan\zeta_2)$ is the position of the bottom of the slope and $x_{lc} = x_b - 30/\tan\zeta_2$ is left coast of the reservoir. Initially, the left end of the reservoir $x = x_{lc}$ has the water height zero, which, due to the slope, gradually increases to its maximum of height of 30 m from the downslope coordinate $x = x_{lc}$ to $x = x_b$. Beyond this (from $x = x_b$ to $x = 300$ m), the initial fluid is at a constant height of 30 m. As the debris moves downslope and hits the fluid reservoir, the generated tsunami will have the amplitude as the increased height of the water from its initial depth of 30 m.
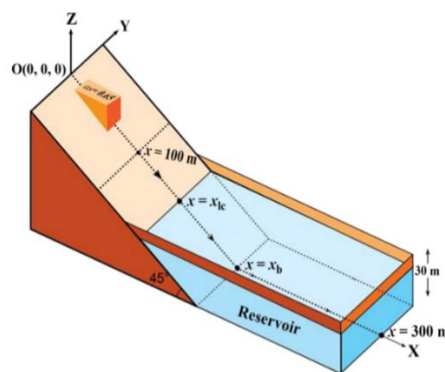
Fig. 3. A sketch of the initial configuration of a debris mass on an inclined slab and a fluid reservoir in the downstream. The figure has been modified from Kafle *et al.* (2016).

Initially at $t = 0$ s, the deformable debris mixture is in the form of a laterally-spanned triangular wedge ($20 \le x \le 70$ m; $-25 \le y \le 25$ m) (Fig.3) which is uniformly distributed as a homogeneous mixture of

65% solid($\alpha_s = 0.65$) and 35% fluid ($\alpha_f = 0.35$). Similarly, the quiescent reservoir initially consists of 2% solid ($\alpha_s = 0.02$) and 98% fluid ($\alpha_f = 0.98$).

Thus, initially, the solid material height (in m) is given by

$$h_s = \begin{cases} 0.65(x - 20), & for\ 20 \leq x \leq 70; \\ & -25 \leq y \leq 25, \\ 0.02(30 - \tan\zeta_2(x_b - x)), & for\ x_{lc} \leq x \leq x_b, \\ 0.02 \times 30, & for\ x_b < x \leq 300, \\ 0, & elsewhere. \end{cases}$$

Similarly, the fluid material height (in m) is given by

$$h_f = \begin{cases} 0.35(x - 20), & for\ 20 \leq x \leq 70; \\ & -25 \leq y \leq 25, \\ 0.98(30 - \tan\zeta_2(x_b - x)), & for\ x_{lc} \leq x \leq x_b, \\ 0.98 \times 30, & for\ x_b < x \leq 300, \\ 0, & elsewhere. \end{cases}$$

The other common parameter values chosen for our simulations are $\phi = 35°$, $\delta = 15°$, $\rho_f = 1{,}100\ \mathrm{kgm}^{-3}$, $N_{R_A} = 1{,}000$, $\mathrm{Re}_p = 1$, $U_T = 5.0\ \mathrm{ms}^{-1}$, $P = 0.75$, $J = 1$, $\chi = 3$, $\xi = 5$, $C = 0.5$. Although this choice of parameters are based on the physics of the two-phase subaerial and submarine mass flows (Pudasaini 2012; Pudasaini 2014; Kafle *et al.* 2016; Kattel *et al.* 2016; Mergili *et al.* 2017), the values can vary according to the properties of materials involved and flow situation.

3.2. Simulation Results and Discussions

Using the aforementioned initial geometrical settings and the material parameters, first we present a reference simulation with constant upstream slope of $45°$ as described in Kafle *et al.* (2019). Then, a couple of simulation results are presented by increasing the slopes of the upper part of the upstream plane, and the other results by increasing the slopes of the lower part of the upstream plane. The results are compared with the reference simulations and also with each other.

3.2.1 Constant upstream slope $(\tan 45°)$

Figure 4 presents a basic simulation for the total debris depth along with the reservoir with tsunami, and also the separate evolution of the solid phase, the penetration of the debris into the reservoir, and the debris-reservoir interaction similar to those presented in (Kafle *et al.* 2016) and (Kafle *et al.* 2019).

As soon as the debris flow is triggered, ($t = 0$ s, left panel a), the debris mass starts to shear both downslope and across. Due to this, the subaerial debris depth substantially decreases as shown by the colour bars given alongside of each panel. In Fig. 7-Fig. 8, the arrows in the top panels represent the flow direction. At $t = 1$ s, the maximum of the debris depth shifts quickly from the front to the main body. As the

shearing continues, the debris depth becomes much lower than the reservoir height at $t = 3$s. The flowing mass already hits the centre of the left coast of the reservoir ($x_{lc} = 170$ m) to generate a tsunami at about $t = 5$s (left panel d) that propagates immediately downslope and across. Since the debris mass further hits the reservoir with higher momentum, the tsunami is expanded in the vicinity of the impact ($t = 7$s, left panel e). As more fluid mass from the left of the reservoir is strongly pushed forward and laterally during the flow, it produces a strong hydrodynamic impact vacuum (Pudasaini 2014), or crater (Fritz *et al.* 2003) at t=9s. For $5 \leq t \leq 9$ s, amplified three-dimensional tsunami waves are observed along with the three complex phenomena (Kafle *et al.* 2016): (i) a subaerial debris flow in the upstream region, (ii) submarine debris flow in the reservoir, and (iii) a tsunami (on the order of 10 m) on the surface of the reservoir. The colour map indicates that the tsunami has propagated in all directions. The debris mass totally enters the reservoir nearly at $t = 9$s. The effect of the impact still persists even in $t = 9$s, showing impact vacuum during the splash.

As the fluid-only and the total geometric evolutions are qualitatively similar due to the dominant fluid volume in the reservoir, we do not show the fluid behaviour separately. However, the dynamics of the solid phase (Fig. 4B) is drastically different, mainly in the reservoir as a submarine mass movement. As the initial debris mass collapses, the front rarefies and accelerates downstream mainly due to the pressure gradient and gravity, whereas the rear part takes some more time to spread and to slide downslope due to the friction and the hindrance of the rear part by the flow front. However, from $t = 1$s (right panel b) to $t = 3$s (right panel c), the position of the relative maximum depth has shifted a bit upslope. At $t = 5$s (right panel d), the maximum depth position is shifted downslope as the initial solid mass in the rear part has moved downslope. In Fig. 4B, maximum solid depth has continuously decreased from 30m at $t = 0$s to around 3.5m at $t = 5$s by its spreading, and increased to a bit more than 7m at $t = 7$s because of the beginning of the solid deposition process. The deposition process continues to $t = 9$s as shown by the further increase of the solid depth to nearly 11m. As the elongated solid tail that appeared in the previous time slices has already shortened and accumulated almost in the solid head, we stop the simulation at $t = 9$s. Due to the impact of the subaerial debris on the reservoir, the solid mass has also been sheared and elongated cross-wise from the front to the middle portion ($t = 5$s, right panel d), where the impact has influenced the dynamics. The lateral boundaries of the reservoir have no significant effect on the lateral shearing. Due to the impact, the lateral spreading of the solid mass has increased from $t = 5$s (right panel d) to $t = 9$s (right panel f). At $t = 8$s, the solid debris part has just crossed the coastal line (x = 170m), which is not shown here. We also observe that the sliding mass changes its geometrical shape by its deformation mainly after it hits the fluid
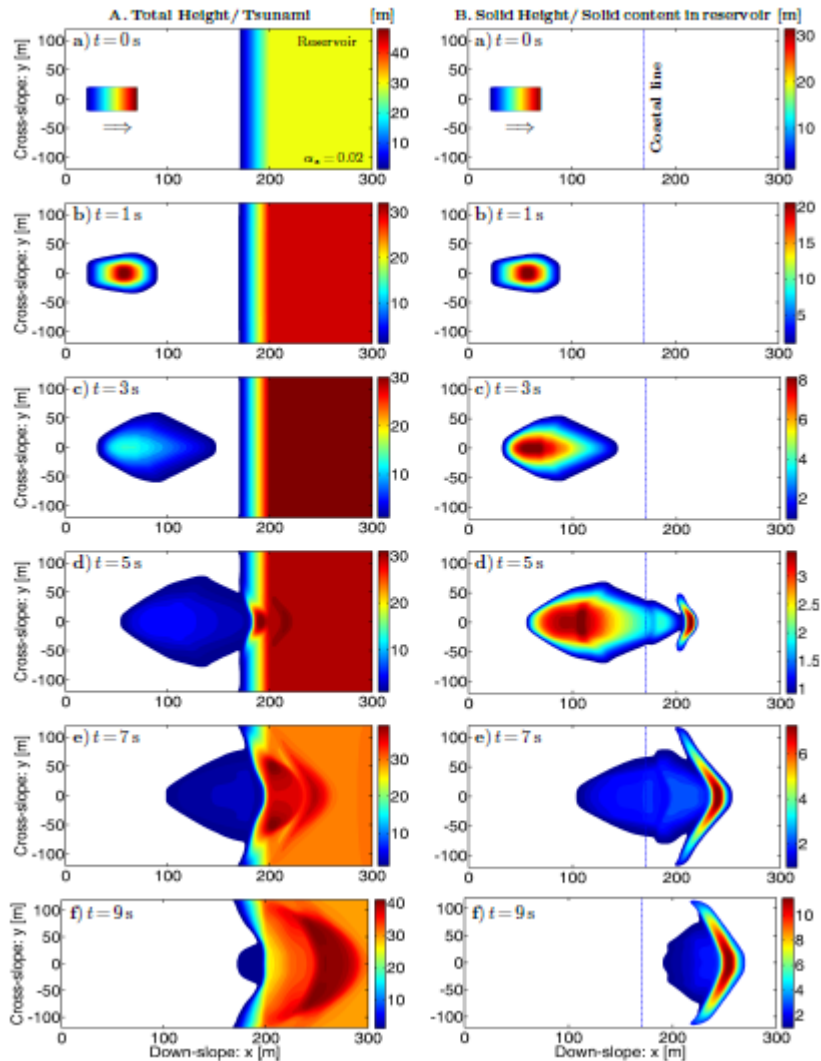
Fig. 4. Constant topographic slope. A: Total height of the debris mass and tsunami waves. As time elapses, the formation, amplification and propagation of three-dimensional tsunamis are observed as subaerial two-phase debris mass impacts the quiescent water reservoir. B: Evolution of the solid phase alone in the debris mixture. As soon as mass is released, the front rarefies and accelerates. After t = 5 s, the solid mass forms a very special forward propagating laterally wide and curved wave of solid component (solid-wave). The vertical line in blue at $x = x_{lc}$ (= 170 m) indicates the left coast of the reservoir (Kafle *et al.* 2019).

reservoir at t = 5s. The impact of the solid mass on the fluid reservoir, from t = 5s to t = 9s (right panel) leads to the formation of a very special for ward propagating laterally wide and curved solid-wave.

Using this as the reference simulation, next we perform some other simulations by varying the slopes in different parts of the upstream sliding plane. First we vary the slopes of the upper part, and in the other set of computational experiments, we vary the slopes of the lower part.

3.2.2 Variation of the Slopes of the Upper Part of the Upstream Plane

Due to some previously occurred landslides and the upstream moving shock during deposition, the

topography might change such that the upper part of the flow path gets steeper than its lower part. To capture this potential realistic scenario, we perform a couple of computational experiments keeping all the material and geometric parameters the same as those in Fig. 4, except we increase the slope of the upper part of the upstream plane.

A. Sudden slope change to $\tan 60^{\circ}$ **:** Figure 5 presents the simulation result when the plane is inclined at 60° for $x \leq 100$m and suddenly the inclination is changed back to 45° for 100m $< x \leq x_b$ (= 200m, up to the bottom of the reservoir). The slope of the upper part of the upstream plane is higher as compared to Fig. 4. As the gravity force is
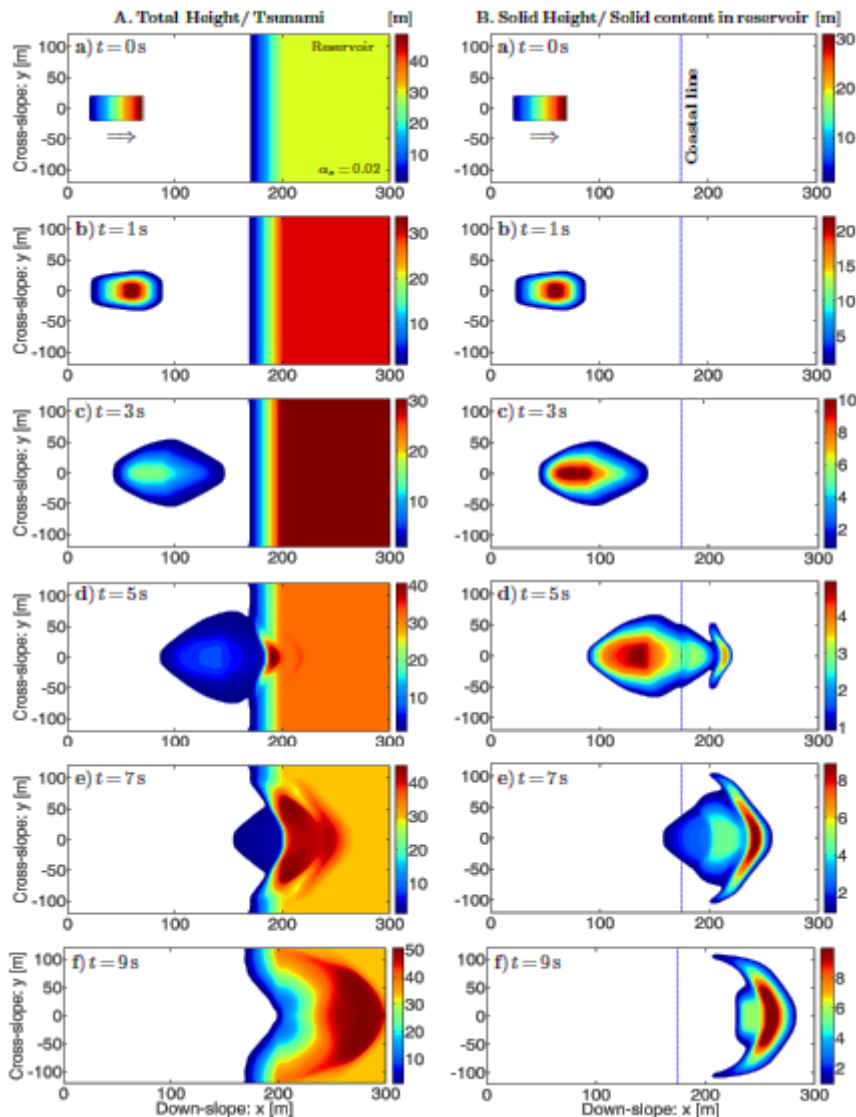
Fig. 5. Sudden slope change of the upper part of the upstream plane from $\tan 45^\circ$ to $\tan 60^\circ$. A: Total height of the debris mass and tsunami waves when the topography is inclined at 60° for $0 \leq x \leq 100m$ and suddenly the inclination is changed back to 45° for $100m < x \leq x_b = 200m$. B: Evolution of the solid phase alone in the debris mixture. Due to the increased slope, the produced tsunami is more intensified and travels longer distance downstream. The vertical line in blue at $x = x_{lc}$ (=170 m) indicates the left coast of the reservoir.

increased, velocity of the debris mass is increased. Because of this, the debris mass hits the left coast of the reservoir already at t = 4s in Fig. 5A, but it occurred only at t = 5s in Fig. 5A . Amplitudes of the tsunami waves are of 10m, 25m and 20m in Fig. 5A whereas they were of just 1m, 8m and 10m (approximately) in Fig. 4A at t = 5s, 7s and 9s, respectively. This is because the debris mass with higher momentum produces higher degree of splash on impact with the reservoir so as to produce tsunami waves with higher intensity.

On analyzing the dynamics of the submarine mass (solid mass inside the reservoir) in Fig. 5B, we notice that the solid mass also moves faster as compared to that in Fig. 4B. At t = 7s, solid mass is almost

submerged in Fig. 5B whereas a considerable portion of the solid mass is still in the subaerial slope in Fig. 4B. So, we observe that submerged time is decreased when we increase the slope or the inclination of the upper part of the sliding plane. The results demonstrate the strong impact of the sudden slope change of the upstream sliding plane, especially in the formation and propagation of very special and dynamically different solid- and fluid-structures in the reservoir.

B. Sudden steeper slope change to $\tan 75^\circ$: When the upper upstream inclination is increased to steeper value (75°) than the previous cases, but keeping the
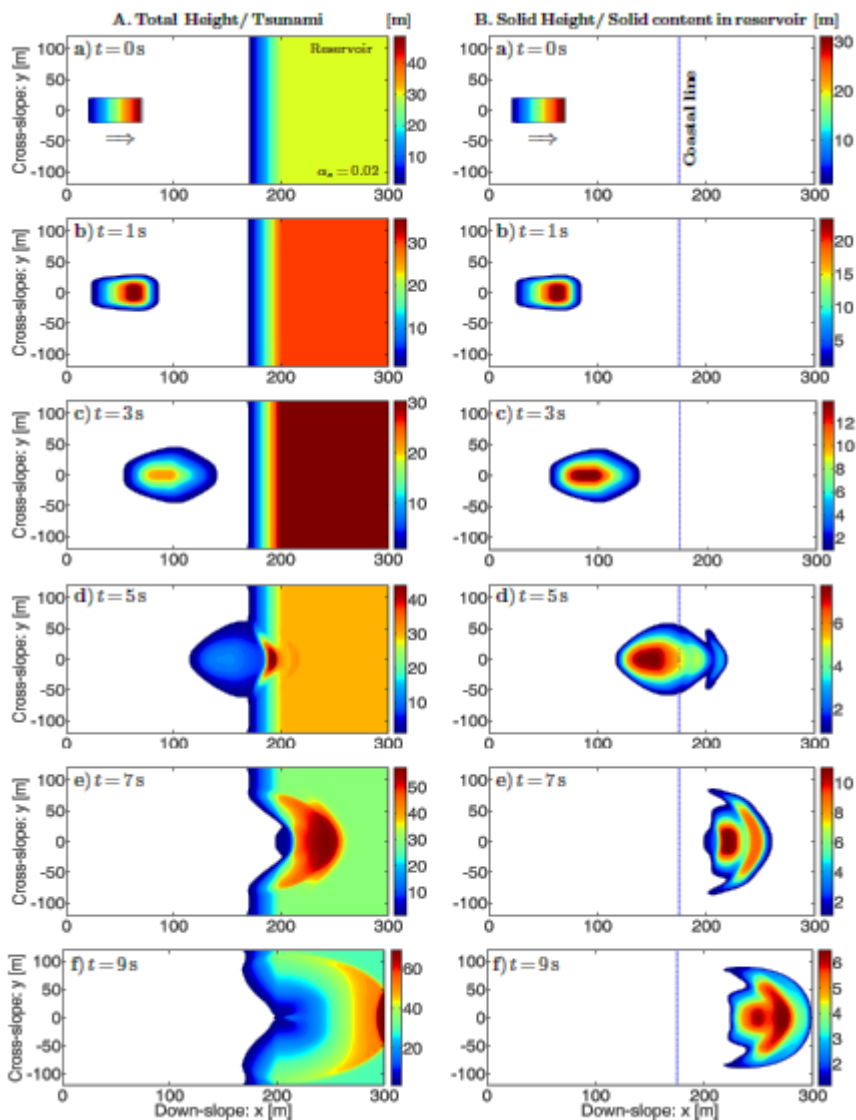
Fig. 6. Sudden steep slope change of the upper part of the upstream plane. A: Total height of the debris mass and tsunami waves when the sliding plane is inclined at $75°$ for $0m \leq x \leq 100m$, and suddenly the inclination is changed back to $75°$ for $100m < x \leq x_b = 200m$. B: Evolution of the solid phase alone in the debris mixture. Tsunami intensity and downstream propagation further increase. The vertical line at $x = x_{lc}$ (=170 m) indicates the left coast of the reservoir.

inclination of the lower part constant (i.e., $75°$), the landslide or debris mass accelerates more rapidly due to the more increased gravity force in the upper part (Fig. 6). This produces even higher impact on the reservoir producing more largely intensified tsunami (of amplitudes 22m, 25m, 38m at t = 5, 7 and 9s respectively) as compared to the previous cases. It is because the larger amount of the transported debris mass with higher mobility transfers higher energy to the fluid in the reservoir on impact. The tsunami propagates more downslope than cross-slope and has already crossed the right coast of the reservoir at t = 9s. As the mechanically stronger solid-rich submarine mass hits the right coast of the reservoir at t = 9s, there is possibility of breaching the right coastal dam, threatening downstream population. To mitigate such potential hazard, installing submarine

obstacles can be useful by decreasing the tsunami propagation, thereby decreasing the submarine mass impact on the right coast of the reservoir. For details, one can refer to Kafle *et al.* (2019).

At t = 7s, the solid mass already gets totally submerged in the reservoir in Fig. 6B whereas some parts of the flowing debris mass were still in the subaerial slope at this time slice in the two previous cases (Fig. 5B and Fig. 4B). Debris mass is more mobile with decreased submerged time when we increase the slope of the upstream part. At t = 7s, a cross wise elongated local maxima is followed by the other maximum which is more localized. The solid phase also advects more downslope in Fig. 6B than in Fig. 5B and Fig. 4B. The front position of the solid mass are at the downslope distances of x = 260m, x = 280m, x = 300m in Fig. 4, Fig. 5 and Fig. 6B

respectively at t = 9s. This leads to completely different dynamics and depositional behaviour of the submarine landslide for a more steeply changing upstream slopes as compared to those with lower slopes. This implies that it might be dangerous to make civil structures around the banks of the water bodies surrounded by mountain flanks with steep upstream slopes.

Next, we vary the slope of the lower part of the sliding plane, analyze the results and compare them with the constant slope and the variation of the slopes of upstream plane.

3.2.3 Slope Variation in the Lower Part of the Upstream Plane

In a natural topography, we sometimes observe that the inclination of the lower part of upstream plane is greater than the upper part due to some construction of civil structures or due to erosion in the bottom part of the flanks due to the water waves. To model this situation, we present a pair of computational experiments when the lower part of the upstream slopes $(100m < x \le x_b)$ are increased to $\tan 60^\circ$ and $\tan 75^\circ$.

A. Sudden slope change to tan 60°: Figure 7 describes the evolution of the debris bulk, the resulting tsunami and the solid portion of the debris mass when the lower part of the upstream plane is increased to $\tan 60^\circ$ $(100\text{m} < \text{x} \le \text{x}_b = 157.73\text{m})$. In this case, the debris mass is more accelerated as it flows downslope in the lower part of the upstream plane. However, this geometrical orientation shifts the left coast of the reservoir to some distance upstream $(x_{lc} = 140.41m)$ as compared to the previous cases. Because of this, it is interesting to observe that the debris mass already hits the left coast of the reservoir at t = 3s, whereas in Fig. 4, the debris mass was yet much further upstream from the left coast of the reservoir. At t = 5s, larger impact force of flowing debris mass produces higher intensity tsunami (10m) in Fig. 7 as compared to the case of the constant slope of the upstream plane (Fig. 4). As a kink is formed due to the sudden slope change in the lower part of upstream slope, the intensity of tsunami is amplified. In Fig. 7 at t = 9s, the debris mass is yet to reach the right coast of reservoir (x = 290m), but in the previous cases it had already hit the right coast of the reservoir. This change in the geometry makes the reservoir longer so that the debris travels along the submarine environment earlier than the previous cases. This change in dynamical interaction of the debris with the reservoir dissipates more energy. This results in the shortening of the run out distance.

In Fig. 7B, we observe that the submarine mass is less mobile along the reservoir basin due to the drastic change of inclination from 60° to 0° during the transition of the topography from the inclined plane to the horizontal bottom $(x_b = 157.73\text{m})$. At t = 9s, two weakly separated local maxima are observed in the cross-slope direction. The solid part of the debris mass is more elongated across in Fig.7B as compared to the previous figures (Fig. 4B - Fig. 6B). This geometrical change in the slope topography can be an effective measure to decrease the tsunami and the submarine mass impact downslope.

B. Sudden rapid slope change to $\tan 75^\circ$: When the lower upstream plane $(100\text{ m} < \text{x} \le \text{x}_b = 126.79\text{m})$ is increased to 75° by keeping the upper part of the upstream plane $(0\text{m} \le \text{x} \le 100\text{m})$ constant, the landslide mass although accelerates more in Fig. 8 than in Fig. 4 and Fig. 7, the tsunami and the submarine mass runouts both decrease in length. The major portion of the sliding debris mass already hits the left coast of the reservoir $(x_{lc} = 118.75m)$ earlier (at t = 3s) in comparison to all the previous cases, where the sliding debris mass was yet to strike or had just started to meet the left coast of the reservoir. In this case, the tsunami of high amplitude (10m) is created even at t = 3s that later propagates less downslope but more cross slope. The early warning system can be more effective in this slope change.

The front of the flowing debris mass is at 275m at t = 9s in Fig. 8A, whereas it was at 290m in Fig. 7A and had just reached the right coast of reservoir in the Fig. 4A. Here, we observe that when we increase the slope of the lower part of the upstream plane, the runout distance of the debris mass is substantially decreased. In this geometrical setting of the slope and reservoir, energy dissipates more, and so there is less risk of dam breaching at the right coast than in other cases. As the tsunami and submarine mass are farther upstream in this case, there is less threat to the downstream population and infrastructure as compared to the previous cases. In Fig. 8B, two cross wise elongated frontal local maxima are followed by one strong and centralized local maximum at t = 5s.

Unlike in the previous cases, the solid phase reveals three localized maxima, two at the front and one at a bit back at 7s and t = 9s. The cross-slope elongations of the solid front occurred mainly at t = 7s and t = 9s. The major portion of the solid mass is accumulated near to the bottom of the slope (t = 5 to t = 9s). Such results may be extended and applied to hazard mitigation and to design less hazard-prone reservoirs for recreation and hydroelectric power generation.

Our results show that the variations in the slopes of the upper and the lower upstream parts of the topography give rise to different flow dynamics of the landslide, impacts on the reservoir, production and propagation of differently intensified tsunami, and different deposition morphology of the submarine mass. These results may help for the proper modeling of landslide and debris induced mountain tsunamis or water waves in rapidly changing slopes, the dynamics of turbidity currents and highly concentrated sediment transports in fluid reservoirs in high mountain slopes, channels, and reservoirs.
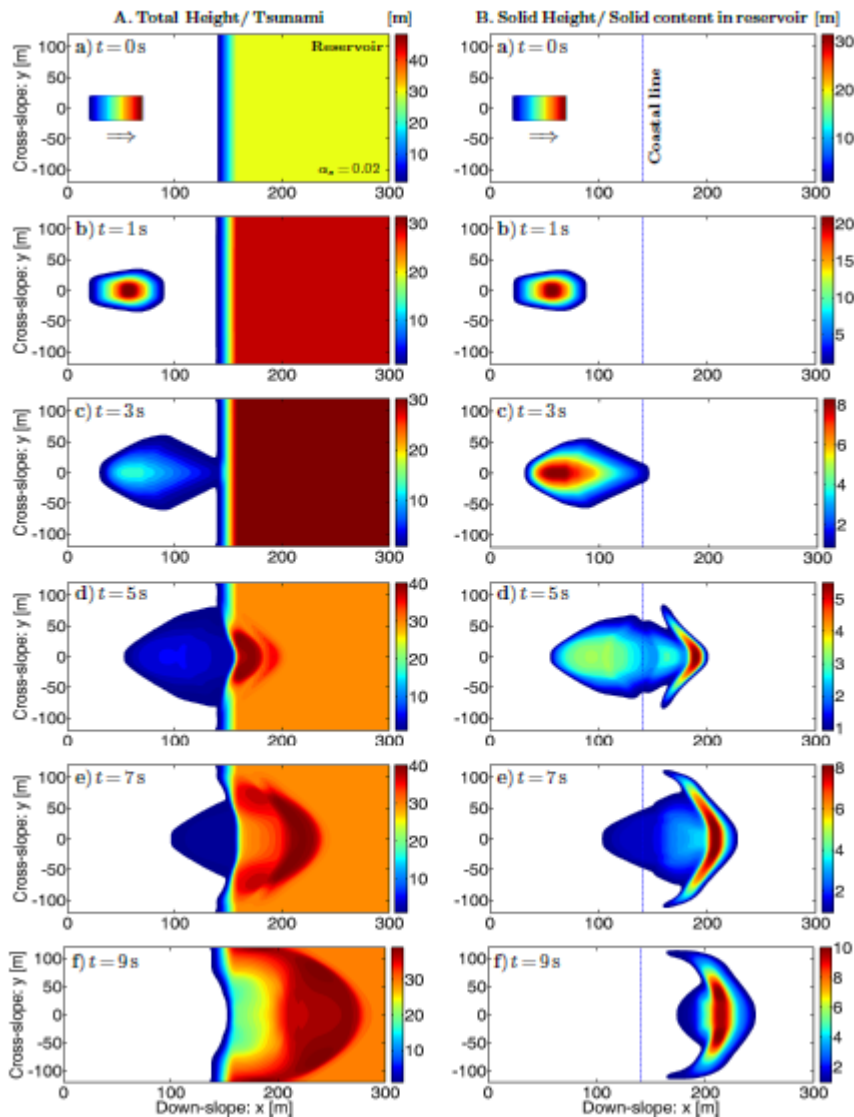
Fig. 7. Sudden slope change of the lower part of the upstream slope. A: Total height of the debris mass and tsunami waves when the topography is inclined at $45°$ for $x \leq 100m$, and suddenly the inclination is increased to $60°$ for $100m < x \leq x_b = 157.73m$. Due to the larger gravity force, the debris mass hits the left coast of the reservoir with higher impact force, and so the tsunami is more intensified than in Fig. 4. B: Evolution of the solid phase alone in the debris mixture. The vertical line in blue at $x = x_{lc} (= 140.41m)$ indicates the left coast of the reservoir.

3.24 Comparisons of Tsunami Amplitudes and Solid Front Positions

Now, we compare the time evolutions of the tsunami amplitudes and the front positions of the solid phase in the different simulations presented in Fig. 4 - Fig. 8. We have taken into accounts of the outputs of other times also in the plots of Fig. 9. In Fig. 9 (Left), we compare the amplitudes of the fluid waves. In the reference simulation with constant upstream slope with inclination $45°$ (Fig. 4), the highest tsunami amplitudes are of approximately 9m (at around x = 200m) and 10m (at around x = 250m) at time t = 7s and t = 9s respectively. When the upper part of the upstream plane in different simulations are made

steeper by keeping the lower part with constant slope (Fig. 5 and Fig. 6), the waves begin to generate almost from the same time but with higher amplitudes. On comparing Fig. 4 -Fig. 6 we observe that the tsunami amplitudes increase along with the slopes of the upper part of the upstream plane as time progresses. The increase of the inclination of $15°$ has doubled the maximum amplitudes at t = 9s. On contrary, the maximum amplitudes are observed to be nearly the same when the lower parts of upstream plane are made steeper keeping the slope of the upper part constant. Since the flow impacts the lake less farther downslope, the waves begin to generate and acquire the maximum amplitudes at early times (nearly at t = 3s in Fig. 7and at t = 5s in Fig. 8).
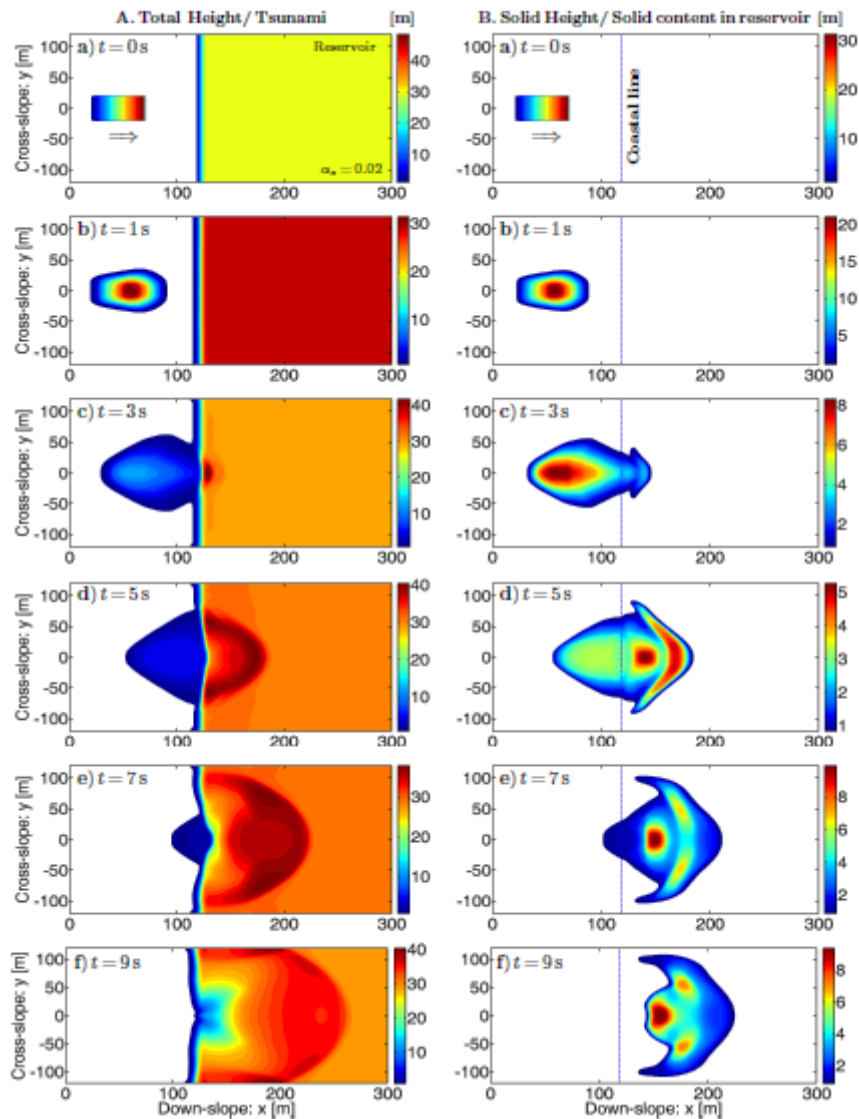
Fig. 8. Sudden steeper slope change of the lower part of the upstream plane. A: Total height of the debris mass and tsunami when the sliding plane is inclined at $45°$ for $0m \leq x \leq 100m$ and suddenly the inclination is changed to $45°$ for $100m < x \leq x_b = 126.79m$. Due to even higher impact of the reservoir by debris mass, the magnitude of the tsunami is more intensified than the previous cases. B: Evolution of the solid phase alone in the debris mixture. At t = 7 s, a relative maximum is at the back and two separated relative maxima are at the front of the solid-part. The vertical line in blue at $x = x_{lc}$ (= $118.75m$) indicates the left coast of the reservoir.

Later, the amplitudes begin to decrease slightly as time progresses. However, in case of Fig. 8, the amplitude slightly increases after t = 7s as the waves begin to localize at the lateral boundaries. In Fig. 6A, when the inclination of the upper part of the upstream plane is increased to $75°$, the amplitude increases rapidly by nearly $(((40-10)/10) \times 100\% =)$ 300% whereas in Fig. 8A when the lower part of the upstream slope is increased to $75°$, the tsunami amplitude is nearly same to the reference simulation with constant upstream slope (Fig. 4). Fig. 9 (Right) presents the comparison of solid front positions downslope for the different configurations (Fig. 5-Fig. 8) among themselves and also with the reference

simulation Fig. 4A (constant upstream slope) from t = 0s to t = 9s. Initially, for all the simulations, the front position is at x = 75m. As the flow is triggered, it moves downslope. In due course of the flow, due to different slopes of the sliding plane, the solid maxima evolve differently and lie at different downslope and cross-slope positions at the sliding plane and the reservoir. On comparing the solid front positions, they move downslope along with the time elapses. As the slope increases in the upper part of the upstream plane, the solid front accelerates more due to the increased gravity and so it reaches farther downslope (nearly at 280m in Fig. 5 and at 300m in Fig.6) at t = 9s. Instead if the slope of the lower upstream plane is increased (Fig.7 and Fig. 8 the flow
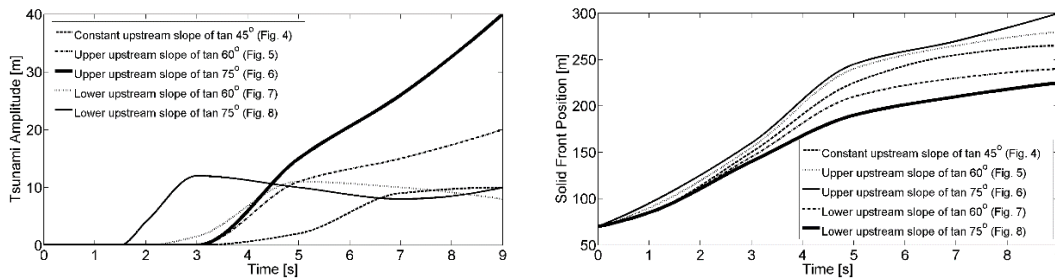
Fig. 9. Left: Comparison of tsunami amplitudes Right: Comparison of solid front positions for different slope variations at t = 0 and t = 9 s.

gets less space to increase its momentum in the subaerial slope and it impacts the reservoir earlier. Because of this, the solid front travels less farther downslope. On comparing the solid front positions with that in the reference simulation (Fig.4), it advects further in Fig. 6 by $((300 - 265) / 265) \times 100\% \approx 13.2\%$ and it lags in Fig.8 by $((265 - 225) / 265) \times 100\% \approx 15.1\%$. The simulation results show that tsunami amplitudes and runout extents are rapidly increased when the upper part of the upstream plane is increased (See, Fig.9). In this case, there is danger of the possible dam break downstream, threatening downstream coastal population and infrastructures. Moreover, runout extent is rapidly decreased when the lower part of the upstream slope is increased (See, Fig.9). In this case, the mobility of both tsunami and submarine mass are substantially decreased by reducing the destructive wave impact, runup and the resulting damages. However, the threats in lateral directions increase since water waves are redirected more across than downslope. These simulation results clearly demand stronger right coastal walls in case of steeper upper part of the topography, and stronger lateral walls in case of the steeper lower part of the topography. Thus, the study of the effects of variation of the slopes of the topography in different parts can be useful for the mitigation of the hazard posed by tsunami and submarine mass movements for the coastal and mountain population and infrastructures.

4. CONCLUSION

The general two-phase debris flow model together with unified high resolution computational tool have been implemented to study the landslide and induced tsunami for the constant and varying slopes of the topography. The results demonstrate strong influence of the sudden slope changes of the topography in the formation and propagation of tsunami and the dynamics of submarine mass when landslide or debris flow impacts still water body. This leads to completely different dynamics and depositional behaviour of the submarine landslide for more steeply changing upstream slopes as compared to those with lower slopes. Through numerical experiments, we suggested that it might be dangerous to make civil structures around the banks of the water bodies surrounded by mountain flanks with steep upstream slopes. When we increase the slope of the lower part of the upstream plane, the

runout distance of the debris mass is substantially decreased. It is due to the large energy dissipation of the debris mass inside the water reservoir. This geometrical arrangement of the slope and the reservoir is useful to prevent the submarine debris mass to breach the right coast of the reservoir. The results also show that the variation of the slopes of the upper and the lower upstream parts of the topography cause different flow dynamics of the landslide, impacts on the reservoir, produce different tsunami intensity and propagation, and possess different deposition morphology of the submarine landslide. The results can be used for the proper modeling of landslide and debris induced mountain tsunamis in rapidly changing slopes, to study the dynamics of turbidity currents and sediment transports in fluid reservoirs located in mountain slopes.

REFERENCES

Behroozi, A. M. and M. Vaghefi (2020). Radial basis function differential quadrature for hydrodynamic pressure on dams with arbitrary reservoir and face shapes affected by earthquake. *Journal of Applied Fluid Mechanics* 13(6), 1759 –1768.

Douglas, S. (2016). *Numerical Modeling of Extreme Hydrodynamic Loading and Pneumatic Long Wave Generation: Application of a Multiphase Fluid Model*. Ph. D. thesis, University of Ottawa, Canada.

Fritz, H. M., W. H. Hager and H. E. Minor (2003). Landslide generated impulse waves .2. hydrodynamic impact craters. *Experiments in Fluids* 35, 520–532.

Grilli, S. T., M. Ioualalen, J. Asavanant, F. Shi, J. Kirby and P. Watts (2007). Source constraints and model simulation of the December 26, 2004, Indian Ocean tsunami. *Journal of Waterway, Port, Coastal, and Ocean Engineering* 133, 414–428.

Jiang, L. and P. H. LeBlond (1993). Numerical

modeling of an underwater Bingham plastic mudslide and the waves which it generates. *Journal of Geophysical Research* 98(C6), 10303–10317.

Kafle, J. (2014). *Dynamic Interaction Between a Two-phase Submarine Landslide and a Fluid Reservoir*, M. Phil. thesis, School of Science, Kathmandu University, Dhulikhel, Nepal.

Kafle, J. (2019). *Advanced Dynamic Simulations of Landslide Generated Tsunami, Submarine Mass Movement and Obstacle Interaction*. Ph. D. thesis, School of Science, Kathmandu University, Kavre, Nepal.

Kafle, J. and B. M. Tuladhar (2018). Landslidewater interaction for partially submerged landslide. *Journal of Nepal Mathematical Society* 1(1), 22–29.

Kafle, J. and P. Kattel (2019). Simulations for rotational symmetry through r.avaflow in the general two-phase mass flow model. *Journal of Nepal Mathematical Society* 2(2), 45–60.

Kafle, J., P. Kattel, M. Mergili, J.-T. Fischer and S. P. Pudasaini (2019). Dynamic response of submarine obstacles to two-phase landslide and tsunami impact on reservoirs. *Acta Mechanica* 230(9), 3143–3169.

Kafle, J., P. R. Pokhrel, K. B. Khattri, P. Kattel, B. M. Tuladhar and S. P. Pudasaini (2016). Submarine landslide and particle transport in mountain lakes, reservoirs and hydraulic plants. *Annals of Glaciology* 57(71), 232– 244.

Kattel, P. (2014). *Dynamics of Quasi-Three Dimensional and Two Phase Mass Flows*, M. Phil. thesis, School of Science, Kathmandu University, Dhulikhel, Nepal.

Kattel, P. (2019). *Some Aspects of Multi-Phase Debris Flows: Dynamics, Flow-ObstacleInteractions and Model Construction*. Ph. D. thesis, School of Science, Kathmandu University, Kavre, Nepal.

Kattel, P., J. Kafle, J. T. Fischer, M. Mergili, B. M. Tuladhar and S. P. Pudasaini (2018). Interaction of two-phase debris flow with obstacles. *Engineering Geology* 242, 197–217.

Kattel, P., K. B. Khattri, P. R. Pokhrel, J. Kafle, B. M. Tuladhar and S. P. Pudasaini (2016). Simulating glacial lake outburst floods with a two-phase mass flow model. *Annals of Glaciology* 57(71), 349–358.

Khattri, K. B. and S. P. Pudasaini (2018). An extended quasi two-phase mass flow model. *International Journal of Non-Linear Mechanics* 106, 205–222.

Kuswandi and R. Triatmadja (2019). The use of dam break model to simulate tsunami runup and scouring around a vertical cylinder. *Journal of Applied Fluid Mechanics* 12(5), 1395–1406.

Ma, G., F. Shi and J. T. Kirby (2012). Shockcapturing non-hydrostatic model for fully dispersive surface wave processes. *Ocean Modelling* 43, 22–35.

Ma, G., J. T. Kirby, T. J. Hsu and F. Shi (2015). A two-layer granular landslide model for tsunami wave generation: theory and computation. *Ocean Modelling* 93, 40–55.

Masson, D. G., C. B. Harbitz, R. B. Wynn, G. Pedersen and F. Lovholt (2006). Submarine landslides: Processes, triggers and hazard prediction. *Philosophical Transactions of the Royal Society A* 364, 2009–2039.

Mergili, M., A. Emmer, A. Juricova, A. Cochachin, J.-T. Fischer, C. Huggel and S. P. Pudasaini (2018). How well can we simulate complex hydro-geomorphic process chains? The 2012 multi-lake outburst flood in the Santa Cruz Valley (Cordillera Blanca, Peru). *Earth Surface Processes and Landforms* 43, 1373–1378.

Mergili, M., J. T. Fischer, J. Krenn and S. P. Pudasaini (2017). r.avaflow v1, an advanced open-source computational framework for the propagation and interaction of two-phase mass flows. *Geoscientific Model Development* 10(2), 553– 569.

Miao, H., G. Wang, K. Yin, T. Kamai and Y. Li (2014). Mechanism of the slow-moving landslides in Jurassic Red-strata in the Three Gorges Reservoir, China. *Engineering Geology*.

Mohammed, F. and H. M. Fritz (2012). Physical modeling of tsunamis generated by three-dimensional deformable granular landslides. *Journal of Geophysical Research* 117(C11015), 705–718.

Pitman, E. B. and L. Le (2005). A two-fluid model for avalanche and debris flows. *Philosophical Transactions of the Royal Society A* 363(3), 1573–1601.

Pokhrel, P. R. and S. P. Pudasaini (2020). Stream function-vorticity formulation of mixture mass flow. *International Journal of Non-Linear Mechanics* 121, 103317.

Pokhrel, P. R., K. B. Khattri, B. M. Tuladhar and S. P. Pudasaini (2018). A generalized quasi two-phase bulk mixture model for mass flow. *International Journal of Non-Linear Mechanics* 99, 229–239.

Pudasaini, S. P. (2012). A general two-phase debris flow model. *Journal of Geophysical Research* 117(F03010).

Pudasaini, S. P. (2014). Dynamics of submarine debris flow and tsunami. *Acta Mechanica* 225(8), 2423–2434.

Pudasaini, S. P. and K. Hutter (2007). *Avalanche Dynamics: Dynamics of Rapid Flows of Dense Granular Avalanches*. Berlin, New York: Springer.

Qiao, C., G. Ou and H. Pan (2018). Numerical modelling of the long run out character of 2015 Shenzhen landslide with a general two-phase

mass flow model. *Bulletin of Engineering Geology and the Environment*.

Sammarco, P. and E. Renzi (2008). Landslide tsunamis propagating along a plane beach. *Journal of Fluid Mechanics* 598, 107–119.

Shrestha, A. B., M. Eriksson, P. Mool, P. Ghimire, B. Mishra and N. R. Khanal (2010). Glacial lake outburst food risk assessment of sun Koshi Basin, Nepal. *Geomatics Natural Hazards and Risk* 1(2), 157– 169.

Slingerl, R. L. and B. Voight (1979). Occurrences, properties, and predictive models of landslide-generated water waves. *Elsevier Scientific Publishing Company*, 317–394.

Viroulet, S., D. C'ebron, O. Kimmoun and C. Kharif (2013). Shallow water waves generated by subaerial solid landslides. *Geophysical Journal International 193*, 747–762.

von Hardenberg, W. G. (2011). Expecting disaster: The 1963 landslide of the Vajont dam. *Environment and Society Portal, Arcadia 8*.

Walder, J. S., P. Watts, O. E. Sorensen and K. Janssen (2003). Tsunamis generated by subaerial mass flows. *Journal of Geophysical Research* 108(5), 2236–2255.

Ward, S. N. and S. Day (2011). The 1963 landslide and flood at Vajont Reservoir Italy, a tsunami ball simulation. *Ital. J. Geosci.* 130(1), 16–26.